ISSN 1674-1056
http://cpb.iphy.ac.cn
http://iopscience.iop.org/cpb
中国物理 B
Chinese Physics
中国物理 Chinese Physics B

Ultrasonic sensitivity-improved fiber-optic Fabry-Perot interferometer using a beam collimator and its application for ultrasonic imaging of seismic physical models

Zhi-Hua Shao(邵志华), Xue-Guang Qiao(乔学光), Feng-Yi Chen(陈凤仪), Qiang-Zhou Rong(荣强周)

Citation: Chin. Phys. B . 2018, 27(9): 094218. **doi:** 10.1088/1674-1056/27/9/094218

Journal homepage: http://cpb.iphy.ac.cn; http://iopscience.iop.org/cpb

What follows is a list of articles you may be interested in

Performance analysis of surface plasmon resonance sensor with high-order absentee layer

Qing-Qing Meng(孟庆卿), Xin Zhao(赵鑫), Shu-Jing Chen(陈淑静), Cheng-You Lin(林承友), Ying-Chun Ding(丁迎春), Zhao-Yang Chen(陈朝阳)

Chin. Phys. B . 2017, 26(12): 124213. **doi:** 10.1088/1674-1056/26/12/124213

Gamma-radiation effects in pure-silica-core photonic crystal fiber

Wei Cai(蔡伟), Ningfang Song(宋凝芳), Jing Jin(金靖), Jingming Song(宋镜明), Wei Li(李伟), Wenyong Luo(罗文勇), Xiaobin Xu(徐小斌)

Chin. Phys. B . 2017, 26(11): 114211. **doi:** 10.1088/1674-1056/26/11/114211

Effect of radiation-induced color centers absorption in optical fibers on fiber optic gyroscope for space application

Jing Jin(金靖), Ya Li(李亚), Zu-Chen Zhang(张祖琛), Chun-Xiao Wu(吴春晓), Ning-Fang Song(宋凝芳)

Chin. Phys. B . 2016, 25(8): 084213. **doi:** 10.1088/1674-1056/25/8/084213

High refractive index sensitivity sensing in gold nanoslit arrays

Yuan Jun, Kan Qiang, Geng Zhao-Xin, Xie Yi-Yang, Wang Chun-Xia, Chen Hong-Da

Chin. Phys. B . 2014, 23(8): 084201. **doi:** 10.1088/1674-1056/23/8/084201

Influence of laser linewidth on performance of Brillouin optical time domain reflectometry

Hao Yun-Qi, Ye Qing, Pan Zheng-Qing, Cai Hai-Wen, Qu Rong-Hui

Chin. Phys. B . 2013, 22(7): 074214. **doi:** 10.1088/1674-1056/22/7/074214

SPECIAL TOPIC — Nanophotonics

Ultrasonic sensitivity-improved fiber-optic Fabry–Perot interferometer using a beam collimator and its application for ultrasonic imaging of seismic physical models*

Zhi-Hua Shao(邵志华), Xue-Guang Qiao(乔学光), Feng-Yi Chen(陈凤仪), and Qiang-Zhou Rong(荣强周)†

School of Physics, Northwest University, Xi'an 710069, *China*

(Received 16 May 2018; revised manuscript received 2 July 2018; published online 28 August 2018)

An ultrasonic sensitivity-improved fiber-optic Fabry–Perot interferometer (FPI) is proposed and employed for ultrasonic imaging of seismic physical models (SPMs). The FPI comprises a flexible ultra-thin gold film and the end face of a graded-index multimode fiber (MMF), both of which are enclosed in a ceramic tube. The MMF in a specified length can collimate the diverged light beam and compensate for the light loss inside the air cavity, leading to an increased spectral fringe visibility and thus a steeper spectral slope. By using the spectral sideband filtering technique, the collimated FPI shows an improved ultrasonic response. Moreover, two-dimensional images of two SPMs are achieved in air by reconstructing the pulse-echo signals through using the time-of-flight approach. The proposed sensor with easy fabrication and compact size can be a good candidate for high-sensitivity and high-precision nondestructive testing of SPMs.

Keywords: fiber-optic sensor, Fabry–Perot interferometer, seismic physical model

PACS: 42.81.Pa, 07.60.Ly, 81.70.Fy **DOI:** 10.1088/1674-1056/27/9/094218

1. Introduction

Ultrasonic imaging of seismic physical models (SPMs) can provide us with the structural information and mechanical characteristics of specific objects and fields.[1–4] The SPMs are laboratorial miniature simulation structures according to the proportion of geologic composition and site. As one of the most important techniques for nondestructive detection of SPMs, ultrasonic imaging of SPMs bridges the gap between theories and field-scale experiments, thereby allowing us to study the changes of acoustic response in a nearly ideal setting without a rock matrix. The traditional detection approach usually employs the piezoelectric transducers (PZTs).[5–7] However, there are some inherent drawbacks in these current-driven transducers: the large diameter or length in the millimeter range limits the imaging resolution and the detection sensitivity decreases as the size reduces; the resonant detection mechanism only offers a narrow bandwidth of detection frequency; the ferroelectric component materials are highly sensitive to electromagnetic disturbances, resulting in large systematic noise and signal distortion; the ultrasonic couplant (such as water and water-soluble polymer gel) is essential to enhance the acoustic coupling and improve response sensitivity. One alternative is to search for a different and superior detection mechanism from PZT. As an optical mean for ultrasonic detection, fiber-optic sensors have attracted significant attention due to their distinct advantages, such as compact size, easy fabrication, high precision, multi-functionality, multiplexing, good stability, and immunity to electromagnetic fields.[8–10] These ultrasonic sensors possess high response sensitivities with controllable cross-sensitivity. Both the flexible waveguide structure and stabilized ultrasonic transmission contribute to the single-point ultrasonic detection in electromagnetic circumstances which are difficult to access. For decades, various types of fiber-optic ultrasonic sensors, based on fiber gratings,[11] fiber interferometers,[12] fiber lasers,[13] tapers,[14] and couplers,[15] have been proposed and widely applied to ultrasonic detection.

Fiber-optic Fabry–Perot interferometers (FPIs) have increasing applications in ultrasonic imaging of SPMs due to their unique advantages of micro size, easy fabrication, high precision, and good stability (immune to lowfrequency disturbances).[16–18] In the mainstream, the diaphragm-based FPIs are preferred for their considerable sensitivity and high-frequency response in pressure and acoustic wave measurements. With the ultrasonic waves (UWs) loaded on the diaphragm, the diaphragm vibration causes the length change of the Fabry–Perot (FP) cavity and finally leads the interference spectrum to shift. Most importantly, high sensitivities are always favored in ultrasonic detection, which are largely determined by the material and structure of the designed FP cavity. A variety of optical thin films with low Young's modulus have been developed as the FP reflections, such as graphene,[19] silica,[20] parylene-C polymer,[21] and gold[22] or silver diaphragm.[23] These optical films need to be thin enough (on a nanometer scale or smaller) to achieve significant sensitivities according to the diaphragm deflection

*Project supported by the National Natural Science Foundation of China (Grant Nos. 61735014, 61327012, and 61275088), the Scientific Research Program Funded by Shaanxi Provincial Education Department, China (Grant No. 08JZ58), and the Northwest University Graduate Innovation and Creativity Funds, China (Grant No. YZZ17088).

†Corresponding author. E-mail: qzrong2010@gmail.com

© 2018 Chinese Physical Society and IOP Publishing Ltd

model,[24–26] and most of these approaches require a waterproof packaging technique so that they can work underwater to realize effective ultrasonic coupling and ensure response sensitivity. Zhang *et al.* proposed an FPI ultrasonic sensor by coating a section of hollow core fiber with a 353ND diaphragm. A signal-to-noise ratio (SNR) of 31.22 dB was obtained and interface information could be distinguished in SPM imaging.[27] To enhance the ultrasonic response, Rong *et al.* employed an ultra-thin gold film to sense the weak UWs in air and two-dimensional (2D) SPM images were successfully reconstructed without a water tank.[22] However, these diaphragm-based FPI sensors have their own unavoidable sensitivity limitations in ultrasonic detection because of their assembled fabrications and multilayer structures. On the other hand, a larger ultrasonic response can be expected via the improvement on ultrasonic signal interrogation. Generally, the spectral sideband filtering technique is utilized for high-frequency ultrasonic detection, in which the laser wavelength is held at the linear slope of the interference spectrum to perform intensity-referenced demodulation. Thus, a lager spectral slope contributes to a higher response sensitivity.[28,29] In the fabrication of fiber-optic FPIs, a longer cavity length leads to a smaller free spectral range (FSR) and thus a larger spectral slope. However, the reducing FSR also narrows the effective spectral filtering range, which may bring signal distortion. Meanwhile, owing to the increased light propagation loss, the fringe visibility of the interference pattern is largely reduced, resulting in a poor ultrasonic response. Fortunately, the reported beam collimation in a graded index fiber can be used to effectively reduce the optical loss inside the FP cavity and largely enhance the fringe visibility by reducing the optical divergence angle,[30,31] which contributes to a much steeper spectral slope for highly sensitive sideband filtering. Thus, a fringe visibility-improved FPI using beam collimation may open a new road to the improvement of the ultrasonic sensitivity in SPM imaging.

In this paper, an ultrasonic sensitivity-improved fiber-optic FPI is designed and experimentally demonstrated for ultrasonic imaging of SPMs. The FP cavity comprises a flexible ultra-thin gold film and the end face of a graded-index multimode fiber (MMF), which are enclosed in a ceramic tube. The MMF in a specific length has the capability to collimate the diverged light beam and compensate for the light loss inside the FP cavity. Thus, the fringe visibility of the interference spectrum is significantly enhanced, leading to an increased spectral slope. By using spectral sideband filtering, the sensing structure shows an improved response sensitivity to UWs. Finally, 2D images of SPMs are achieved in air by reconstructing pulse-echo signals using the time-of-flight approach.

2. Sensor fabrication and sensing mechanism

2.1. Sensor fabrication

Figure 1(a) presents a schematic diagram of the fiber-optic FPI sensor. A ceramic ferrule with a 135 μm inner diameter and a 2.5 mm outer diameter is used as a housing tube. One end-face of the ceramic ferrule is firstly coated with a 130-nm-thick gold film. The commercial ultra-thin gold film possesses high optical reflectivity and also deforms significantly under UWs, which is a good candidate for the fabrication of functioned diaphragm-based ultrasonic sensors. Before the coating, the end-face of the ceramic ferrule needs to keep contaminant-free so that it can absorb the gold film by van der Waals force. Although the intermolecular forces are weak, it is strong enough to bond the gold film firmly because of the ultra-thin thickness. Afterwards, a 260-μm-long graded-index MMF with flat cleaved end-faces is spliced to a leading-in standard single mode fiber (SMF) as a beam collimator and then inserted into the center hole of the ceramic ferrule. Thus, an air gap is formed by the fiber end (R1) and gold film (R2), which can be adjusted as needed by changing the insertion depth of the SMF–MMF structure. Finally, the fiber pigtail is bonded to the ceramic ferrule by an epoxy resin adhesive to ensure the structural stability. When the sensor probe is illuminated with a laser source, the input light is partially reflected by R1 and R2, respectively. Due to the phase difference between the two reflections from the air gap, a well-defined FPI probe is achieved for ultrasonic detection as shown in Fig. 1(b). The fibers are all fusion spliced by a Fujikura arc fusion splicer (FMS-60 S), of which the arc discharge condition can be quantitatively controlled. The SMF-MMF structure is spliced under the arc discharge condition of $I = 10.4$ mA and $t = 1.5$ s.

As shown in Fig. 2, the graded-index MMF has a core diameter of 62.5 μm and a cladding diameter of 125 μm. The effective refractive index (RI) of the graded-index fiber continuously decreases with increasing radial distance from the optical axis of the fiber, thus forming a nearly parabolic RI profile. Because part of the fiber core closer to the fiber axis has a higher RI than the part near the fiber cladding, the light beams follow sinusoidal paths down the fiber core, resulting in the continual refocusing of the light beams. The period of the sinusoidal path is defined as the pitch of the MMF. If the fiber length is $n/4$ (n is an odd number) of the pitch, the divergence angle of the light beams from the MMF is the smallest and the output light beams are collimated to be approximately parallel as can be seen from the light propagation in Fig. 1(a). In our previous work, it has been demonstrated theoretically and experimentally that the minimum divergence angle is about 2.55° and the first quarter pitch of the MMF is 260 μm.[30] Since light beams in a step-index fiber experience larger divergence angles and thus higher propagation loss, the 260-μm-long graded-index MMF in Fig. 1(a) can be used as a beam collimator or a quarter-pitch collimator to compensate for the light loss inside the FP cavity and enhance the fringe visibility.

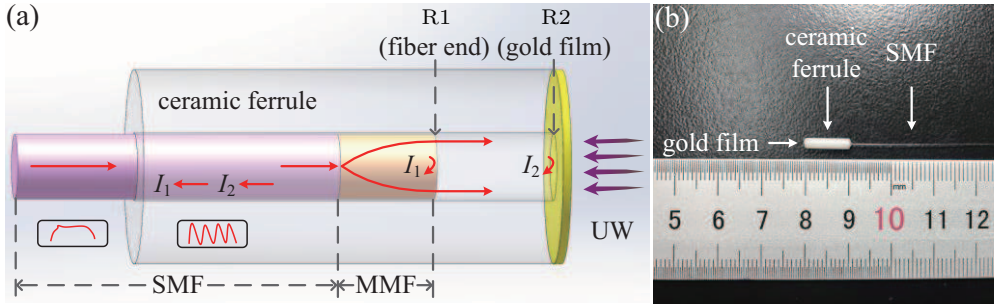


Fig. 1. (color online) Sensor fabrication: (a) schematic diagram of the FPI sensor, (b) photograph of the sensor probe.

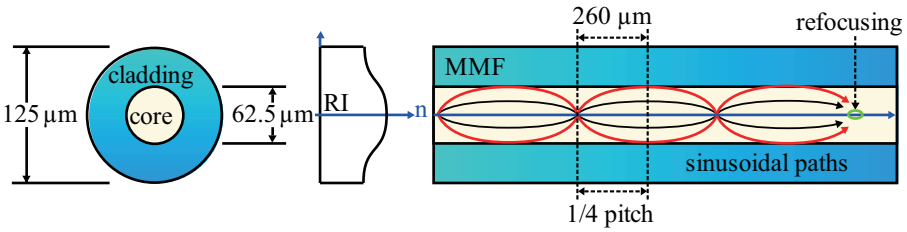


Fig. 2. (color online) Principle of beam collimation in graded-index MMF.

The key of the sensor fabrication is the precise cleaving of the MMF, which can ensure that the output beams are well-collimated. Figure 3 shows a home-built platform for precise fiber cleaving, including a refitted fiber cleaver (Fujikura, CT-32), two 3-axis stages (Thorlabs, MAX313D), and a microscope (Olympus, SZX16). The spliced SMF-MMF structure is mounted on the two stages by fiber holders and meanwhile the middle splicing section is placed on the fiber cleaver with its blade perpendicular to the fiber axis. The two stages enable nanometric positioning on three orthogonal axes to control the fiber length. Moreover, the relative position between the blade and fiber is monitored and aligned by the upper microscope. In the cleaving operation, the splicing point of the SMF–MMF structure is firstly adjusted to coincide with the blade. Then the fiber is pulled with a length of 260 μm along the fiber axis and finally the blade is activated to finish the precise cleaving of the MMF. Besides, the platform in Fig. 3 can also be used for adjusting the length of the FP air cavity. Combining real-time monitoring of the reflection spectrum with a swept laser based optical spectrum analyzer (Micron Optics, SM125-700), we can obtain a desired interference spectrum for spectral sideband filtering.

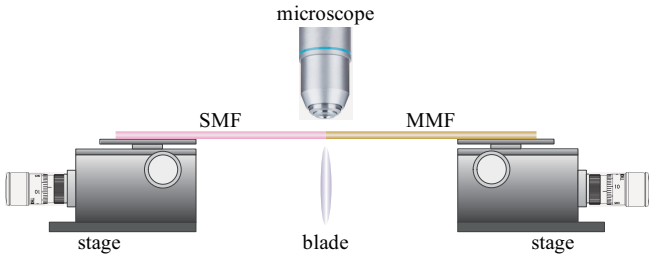


Fig. 3. (color online) Schematic diagram of the platform for precise cleaving and FP cavity adjustment.

The interference spectrum of the proposed sensor is obtained with a cavity length of 233 μm in Fig. 4(a) (the red curve with MMF), which shows an FSR of 5.12 nm, a spectrum loss of −19.65 dB, and an extinction ratio of 28.24 dB. In order to verify the beam collimation inside the MMF, another FPI using one single SMF as the R1 is also fabricated with the same cavity length. The corresponding interference spectrum is profiled with an FSR of 5.34 nm, a spectrum loss of −25.52 dB, and an extinction ratio of 17.11 dB (the blue curve without MMF). By comparison, the two FPIs have approximately the same FSR, but the one with MMF has lower loss and a larger extinction ratio. Furthermore, the fringe visibility is given in terms of the observed intensity maximum $I_{\max}$ and minimum $I_{\min}$ in the interference pattern by

$$V_{\mathrm{FP}} = \frac{I_{\max} - I_{\min}}{I_{\max} + I_{\min}}. \tag{1}$$

Actually, the FPI with MMF has an improved fringe visibility of 0.997 compared with the value 0.961 without MMF. Therefore, by adding a short section of graded-index MMF into the FP cavity, the beam collimation can significantly reduce the light loss and improve the fringe visibility of the interference pattern. Consequently, owing to the close FSRs and different extinction ratios in Fig. 4(a), the interference spectrum with MMF has a larger spectral slope of about 11.2 dB/nm compared to 6.4 dB/nm of that without MMF.

In order to further demonstrate the interference pattern of the collimated FPI, the corresponding spatial frequency spectrum by Fourier transform is presented in Fig. 4(b). When the light beam is injected into the MMF, multiple light modes in different orders are excited due to the MMF's fairly large core diameter.[32,33] As can be seen in Fig. 4(b), the mode interference is mainly attributed to the fundamental mode. The other weak high-order modes participate in modifying the main interference pattern, resulting in the slightly inhomogeneous interference spectrum in Fig. 4(a). Furthermore, another four

probes with different cavity lengths are also fabricated by inserting the cleaved SMF-MMF structure into the ceramic ferrule at different depths. The corresponding FSRs are obtained using the optical spectrum analyzer and plotted versus cavity lengths in Fig. 4(c). The experimental data agree well with the theoretical results (solid line), which are calculated and fitted by employing the typical FSR equation for an FPI[34]

$$\mathrm{FSR} = \frac{\lambda_1 \lambda_2}{2 n_{\mathrm{air}} L}, \tag{2}$$

where λ_1 and λ_2 are the two detected adjacent wavelengths, n_{air} is the effective RI of the air cavity, and L is the length of the air cavity. Therefore, the gold film-based sensor is a well-designed FPI with easy fabrication and reproduction.

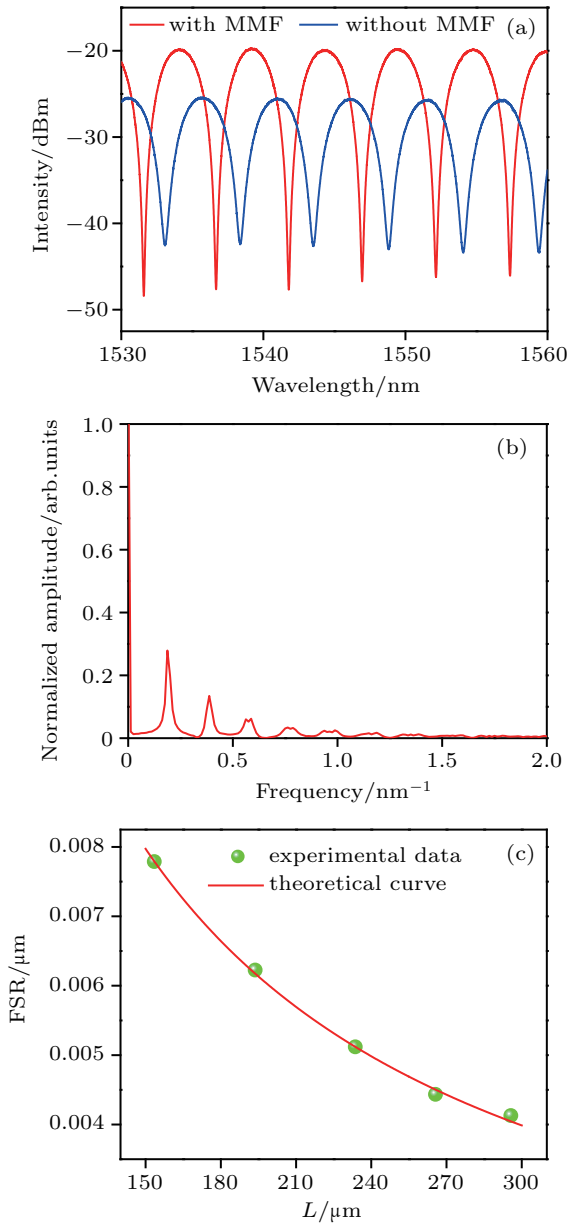


Fig. 4. (color online) (a) Interference spectra with and without MMF, (b) spatial frequency spectrum of collimated FPI sensor, and (c) theoretical and experimental results for FSR versus cavity length L.

2.2. Sensing mechanism

The ultrasonic response of the sensor can be characterized theoretically by analyzing the interaction between the optical interference and UWs. In the detection, the PZT source mainly emits longitudinal waves. Since the UW wavelength (typically 1.13 mm in air for 300 kHz UWs) is much longer than the sensing region of the nano-sized gold film, the UW can be regarded as a plane wave and series of homogeneous ultrasonic expansions and compressions. When the UW is applied to the sensor in air, most of the ultrasonic power is reflected at the air-to-film interface due to the large acoustic impedance difference between the gold film (62.5×10^6 kg/(m^2·s)) and air (0.0004×10^6 kg/(m^2·s)). The interaction force periodically deforms the gold film in the form of axial tension or compression, resulting in the length variation of the FP cavity. Since the flat gold film has a uniform thickness, its center deformation ΔL under the applied acoustic pressure ΔP can be expressed as

$$\Delta L = \frac{3(1-\mu^2) r^4}{16 E h^3} \Delta P, \tag{3}$$

where μ and E are the Poisson's ratio and Young's modulus, and h and r are the thickness and effective radius of the gold film, respectively.[35] The deformation in Eq. (3) significantly determines the length change of the FP cavity, which leads the interference spectrum to shift accordingly. Because the low reflectivity of the fiber end-face (R1), the FPI can be simplified as a dual-beam interferometer. As shown in Fig. 1(a), the optical intensity can be expressed as

$$I = I_1 + I_2 + 2\sqrt{I_1 I_2} \cos \varphi, \tag{4}$$

where I_1 and I_2 are the intensities of the two reflected beams, respectively. $\varphi = 4\pi n_{\mathrm{air}} L/\lambda$ is the phase difference induced by the FP cavity. The phase difference satisfies the resonance condition $\varphi = (2m+1)\pi$ (m is an integer). For the cavity length change ΔL, the wavelength shift of the FPI can be expressed as

$$\Delta\lambda = \frac{4 n_{\mathrm{air}}}{2m+1} \Delta L. \tag{5}$$

By combing Eqs. (3) and (5), the wavelength-referenced acoustic pressure sensitivity of the sensor can be derived to be

$$\frac{\Delta\lambda}{\Delta P} = \frac{3 n_{\mathrm{air}} r^4 (1-\mu^2)}{4 E h^3 (2m+1)}. \tag{6}$$

For optimal sensitivity and linearity by spectral sideband filtering, the sensor works at the quadrature phase bias point where $\varphi = (2m+1)\pi/2$ by tuning the wavelength of the laser source.[36] The UW-modulated wavelength shift is transformed into the variation of the output optical intensity, which is finally amplified and converted into voltage signals. Thus, the change of the output optical intensity ΔI can be expressed as

$$\frac{\Delta I}{\Delta\lambda} = k(\varphi), \tag{7}$$

where $k(\varphi)$ is the spectral filtering slope at the optimum phase bias point.[21] Eventually, the ultrasonic sensitivity, i.e., the reflected optical intensity modulation per unit acoustic pressure, is given by

$$\frac{\Delta I}{\Delta P} = \frac{\Delta \lambda}{\Delta P} \cdot \frac{\Delta I}{\Delta \lambda} = \frac{3 n_{\text{air}} r^4 (1-\mu^2)}{4Eh^3(2m+1)} k(\varphi). \tag{8}$$

Equation (8) clearly reveals that the sensor sensitivity depends on both the structural parameters and the spectral filtering slope of the FPI. The gold film-based sensor has an excellent ultrasonic sensitivity due to the ultra-thin film thickness, and thus it can detect the weak UWs in air, which has been demonstrated experimentally in our previous work.[22] According to Eq. (8), the two FPIs for comparison in Fig. 4(a) have the same wavelength-referenced acoustic pressure sensitivity because of the given gold film. Moreover, the ultrasonic sensitivity of the gold film-based sensor can be further promoted with an increased spectral filtering slope.

Based on the properties of the gold film, the natural frequency can be calculated as follows:[20]

$$f_0 = \frac{10.21h}{4\pi r^2} \sqrt{\frac{E}{3\rho(1-\mu^2)}}. \tag{9}$$

For the given gold film with thickness $h = 130$ nm, radius $r = 67.5$ μm, Young's modulus $E = 78$ GPa, mass density $\rho = 19.3$ g/cm^3, and Poisson's ratio $\mu = 0.44$, the resonance frequency can be calculated to be about 30 kHz. In the ultrasonic imaging of SPMs, the working frequency of the sensor should be close to the resonant frequency to obtain a large ultrasonic response. Therefore, a fixed acoustic emission at 300 kHz, one of the common ultrasonic frequencies in SPM imaging, is used as the ultrasonic source in the following experiments.

3. Sensor response and SPM imaging

The schematic configuration of the fiber-optic sensing system is shown in Fig. 5. A tunable laser beam (Santec, TSL-710) with a 100 kHz linewidth as a light source irradiates on the sensor through an optical circulator, and the reflected light power is converted into an electrical signal by a photodetector (PD) (New Focus, Model 2117) with a bandwidth of 10 MHz and finally recorded by an oscilloscope (RIGOL, DS2302 A). To characterize the sensor in air, the sensor is held on a moving stage, and the PZT source, which is driven by a function generator to emit 300 kHz UWs, is held on a fixed stage. The central axes of the sensor and PZT are kept in the same line parallel to the experiment platform. The distance between the sensor and PZT can be precisely controlled through the moving stage. For SPM imaging, Plexiglas blocks are placed at the bottom of an air tank as the physical models. Meanwhile, the sensor and PZT are separately fixed on a 2D motorized stage over the SPMs to perform point-to-point scanning imaging.

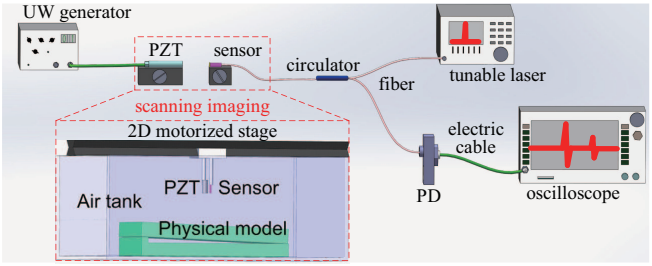


Fig. 5. (color online) Schematic configuration of the experiment setup for ultrasonic detection.

3.1. Ultrasonic response of the sensor

The time-domain response of the collimated FPI to a 300 kHz sinusoidal UW is presented in Fig. 6(a) (the red curve), where the horizontal distance between the sensor and PZT is fixed at 10 cm. This real-time response presents a quasi-sinusoidal profile with a peak-to-peak voltage of 4.02 V. By comparison, the FPI without MMF shows a low ultrasonic response of 1.65 V (the blue curve). To characterize the frequency of the ultrasonic signal, the time-domain curve in red is converted into the frequency domain by taking the Fourier transform as shown in Fig. 6(b). It clearly reveals a single ultrasonic frequency of 300 kHz, which is coincident with the emission frequency of the PZT source.

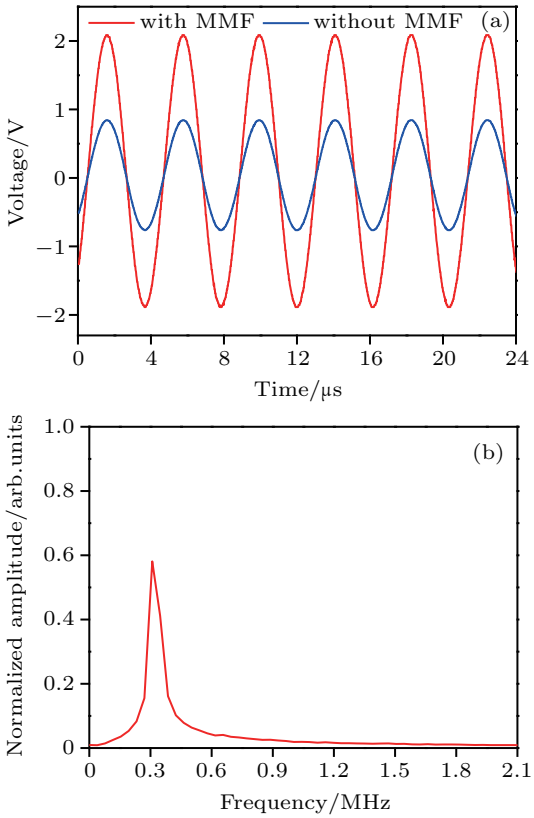


Fig. 6. (color online) Response to a 300 kHz sinusoidal UW: (a) comparison between FPIs with and without MMF in the time domain, and (b) the frequency-domain spectrum with MMF.

The PZT source is further driven by a 300 kHz square-wave pulse. Figure 7(a) shows the time-domain response difference between the two FPIs. The FPI with MMF presents

a higher peak-to-peak voltage of 3.1 V (the red curve) than the value 1.24 V of the FPI without MMF (the blue curve). Because the sensors are characterized in the same experiment setup, here the SNR is proposed to characterize the ultrasonic response. The SNR highly depends on the initial noise of the experimental setups, especially induced by the power fluctuation of the laser source, transmission lines, and sensor stability. Given the noise voltage of 2 mV and the signal peak-to-peak voltages in Fig. 7(a), the SNRs of the two FPIs are calculated to be 63.8 dB (with MMF) and 55.84 dB (without MMF), respectively. Thus, the collimated FPI with a higher SNR is more sensitive to UWs. Furthermore, the time-domain spectrum with MMF in Fig. 7(a) is transformed into the frequency domain as shown in Fig. 7(b). It is seen that the main frequency of the ultrasonic signal is 300 kHz, which agrees well with the emission frequency of the PZT. The low components around the main frequency result from the sensor response to the extra resonant components of the PZT source, which should be filtered out in the image reconstruction of SPMs. The frequency-domain performance also presents that the sensor has a wide frequency band response to UWs.

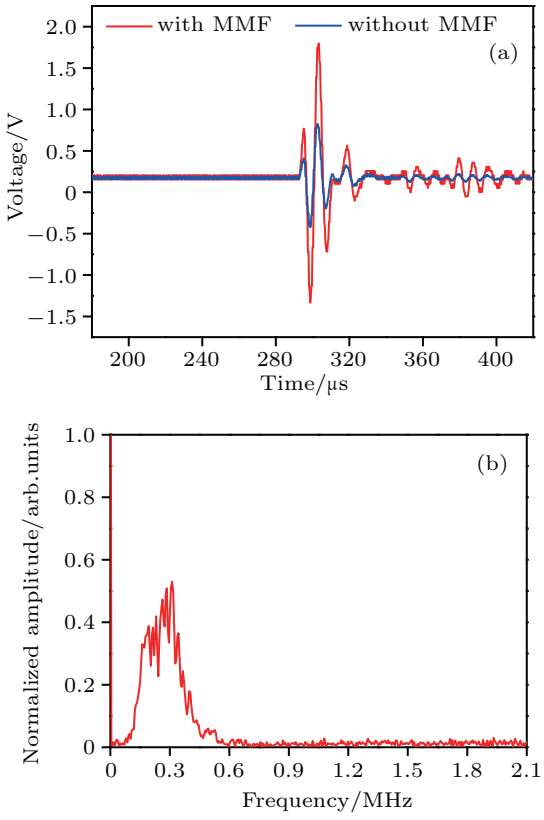


Fig. 7. (color online) Response to a 300 kHz pulsed UW: (a) comparison between two FPIs in the time domain, and (b) the frequency-domain spectrum with MMF.

As the driving voltage of the function generator increases continuously from 50 V to 225 V at 300 kHz, the peak-to-peak voltage of the time-domain signal also increases linearly as shown in Fig. 8(a). The output optical intensity of the sensor, which is converted into an electrical voltage, is proportional to the ultrasonic strain field, which is directly determined by the driving voltage at a fixed frequency. The slight fluctuation of the experimental data may result from the nonlinear increase in acoustic pressure. Furthermore, the detection aperture (the angular range of ultrasonic reception determined by the sensor size) is another key factor. As illustrated in the inset of Fig. 8(b), the sensor displacement varies from −5 cm to 5 cm in steps of 1 cm and the direction angle θ correspondingly changes from −26.5° to 26.5° . The signal voltage presents an orientation-dependent response in Fig. 8(b). The maximum response at 0° is generally adopted in the ultrasonic detection, i.e., the PZT and sensor are face to face in the same line. The data asymmetry may be from the slight asymmetry of the whole displacement process.

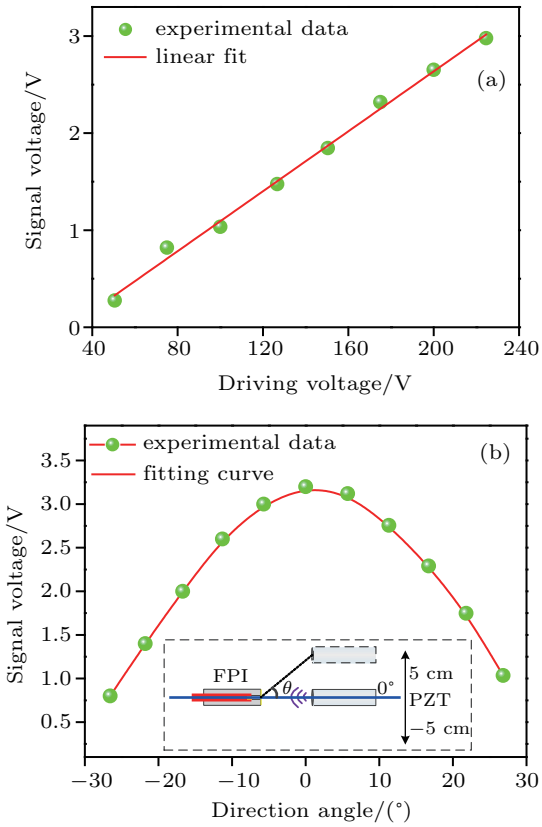


Fig. 8. (color online) (a) Signal voltage versus driving voltage at 300 kHz, and (b) orientation-dependent response from −26.5° to 26.5°.

To demonstrate the sensor stability, a time-domain sequence in response to pulsed UWs is acquired at room temperature as shown in Fig. 9(a). The peak voltages of the response sequence are extracted and distributed in Fig. 9(b) to present their fluctuations. The maximum fluctuation of the peak voltage is only 0.0322 V. Compared with the output voltage of about 1.6 V, this fluctuation can be neglected. Thus, the uniform pulse array confirms the sensor stability. The good stability is mainly attributed to the tunable laser source TSL-710, which has a built-in wavelength monitoring with a high wavelength stability of ±1 pm and power stability of ±0.01 dB. Thus, the output wavelength of the TSL-710 can be well located at the optimum bias point of the interference spectrum for highly sensitive ultrasonic detection.

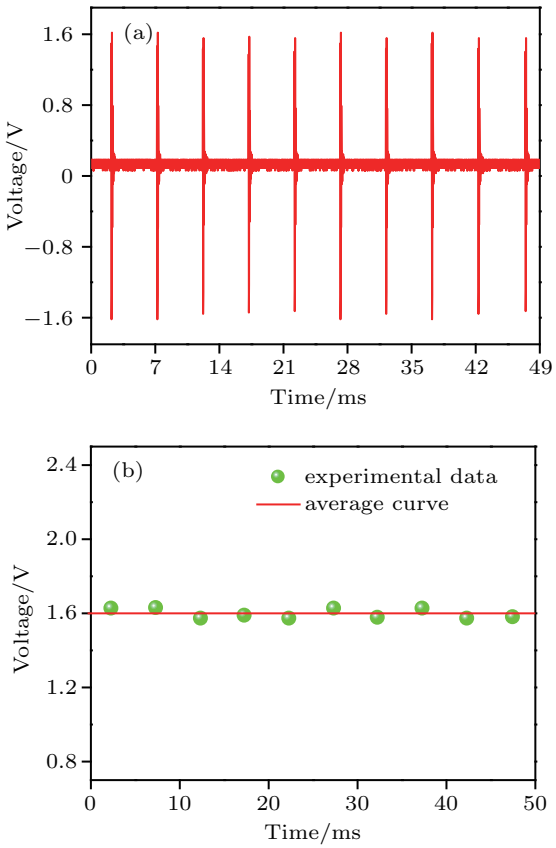


Fig. 9. (color online) Sensor stability: (a) response sequence to a 300 kHz pulsed UW, and (b) fluctuation of output voltage at room temperature.

To characterize the long-term stability, the output voltages are continuously monitored at room temperature. The raw response data per 3 hours in 27 hours are extracted, and the fluctuation of the peak-to-peak voltages versus time is shown in Fig. 10. Compared with the signal peak-to-peak voltage (about 3.2 V), the maximum fluctuation in 27 hours is only about 0.14 V. Thus, our sensor presents a good stability at room temperature and can be used for long-term detection.

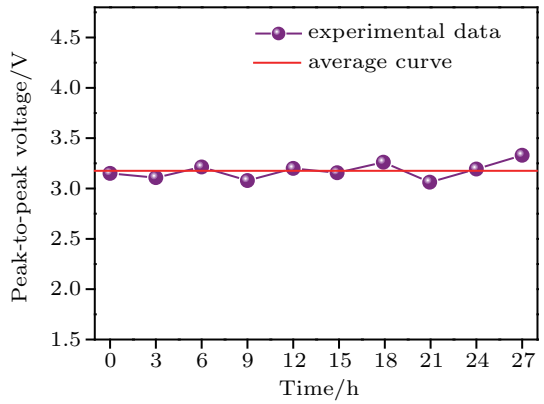


Fig. 10. (color online) Fluctuation of the output peak-to-peak voltage in 27 hours.

3.2. Ultrasonic imaging of SPMs

To perform the SPM imaging, the sensor and PZT are held on the motorized stage with a fixed horizontal separation of 3 cm inbetween, as illustrated in Fig. 5. The SPMs in the tank lie vertically below the two components. Two types of Plexiglas blocks in different shapes are used as the physical models (see Fig. 11). The model in Fig. 11(a) is a tilted rectangular bulk with a thickness of 5 cm and a width of 50 cm. The other in Fig. 11(b) is a solid half-cylinder with a radius of 5 cm. The titled rectangular bulk is used to simulate the geological multilevel stratum, in which the reflected signals by each interface are acquired to reconstruct the layer information. And the solid half-cylinder is machined to simulate the geological uplift, such as the cove and hog, of which the arc surface can be clearly distinguished by scanning imaging. The vertical distance between the sensor and the highest point of the SPMs is about 6 cm. During the scanning operation, the stage is programmed to enable horizontal displacement in steps of 1 mm, and thus the PZT and sensor move quasi-continuously to perform point-to-point scanning. The whole scanning process is implemented in air. The PZT emits pulsed UWs to the SPMs and the sensor detects the pulse-echoes from the SPMs. The UWs are mainly reflected by interfaces between air and the SPMs (upper and bottom surfaces). Partial UWs propagate through the SPMs and reflect due to structural discontinuities inside the SPMs. Given the ultrasonic transmission velocity in air (340 m/s) and Plexiglas (2730 m/s), the values of time-of-flight of the reflected UWs are determined, corresponding to the interface information of SPMs. After signal filtering and amplification, 2D images of the two SPMs can be reconstructed, which indicate the shapes, sizes, and inner structures of the physical models.

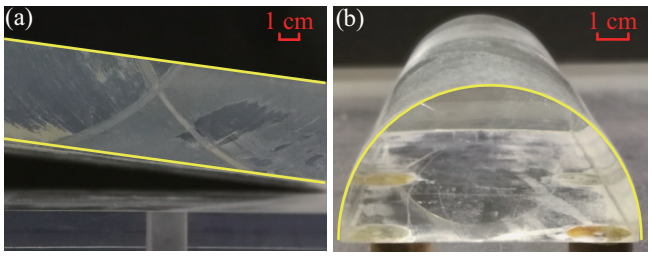


Fig. 11. (color online) Photographs of two SPMs: (a) tilted rectangular bulk, (b) solid half-cylinder.

Figure 12 shows the ultrasonic images of the two SPMs by the time-of-flight approach. For the rectangular model in Fig. 12(a), the upper and bottom surfaces and the tilted angle are clearly imaged, which accord well with the actual model in Fig. 11(a). The image in Fig. 12(b) also gives a clear profile of the solid half-cylinder in Fig. 11(b), including the upper arc surface and the bottom surface. Meanwhile, two distortions are notable: the incomplete bottom surface due to the half-cylinder's focusing effect and the radius extension due to the angular reflection by the upper arc surface. Owing to the large impedance difference between the air (0.0004×10^6 kg/(m^2·s)) and Plexiglas (3.1×10^6 kg/(m^2·s)), the acoustic reflection coefficient can reach up to 99.97% in a certain depth, leading to the much stronger reflection signal of the upper surface in the two images. It is also noted that there are small surfaces appearing between the two main

surfaces. We can consider this phenomenon as a form of reverberation. In the presence of two reflective interfaces, the echoes generated from the main beam may be repeatedly reflected, in repeated trips before going back to the sensor, where they may be detected. Each echo is received erroneously and transcribed as a band located at a greater depth, so we may see multiple parallel lines with different intensities which are are equidistant from each other.

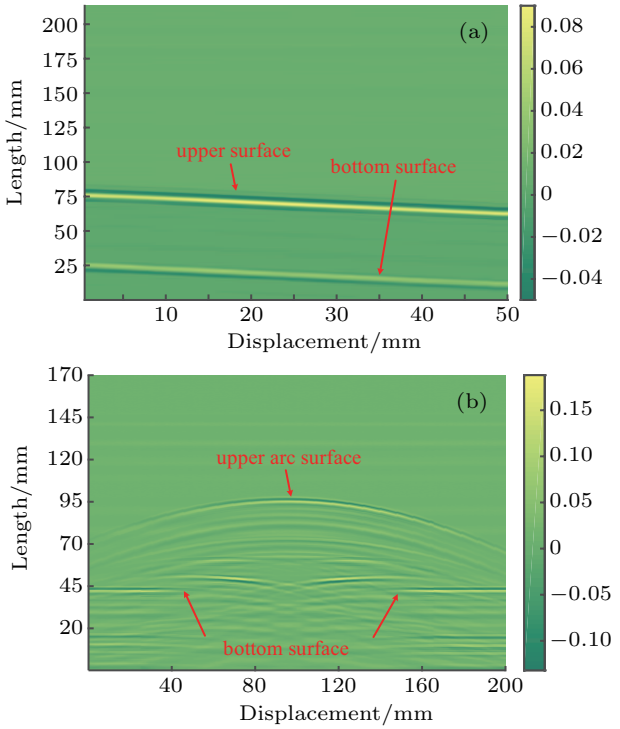


Fig. 12. (color online) Images of SPMs by a time-of-flight approach, showing (a) tilted rectangular bulk, and (b) solid half-cylinder.

Furthermore, the spatial resolution of the sensor R can be estimated from the following two equations:

$$R = 0.61\frac{\lambda_{\mathrm{UW}}}{N_{\mathrm{FPI}}}, \tag{10}$$

$$N_{\mathrm{FPI}} = n_{\mathrm{air}}\sin\theta, \tag{11}$$

where λ_{UW} is the ultrasonic wavelength in air, and N_{FPI} is the sensor detection aperture.[37] Given the ultrasonic frequency used in the experiments (300 kHz) and the sensor direction angle θ in air (-26.5° to 26.5°), the spatial resolution of the sensor can be calculated to be 1.53 mm. Thus, the proposed collimated FPI can enable high-resolution ultrasonic imaging of SPMs.

4. Discussion

In our work, a micro fiber-optic interferometer is developed for ultrasonic imaging of seismic physical models. The laser source (Santec, TSL-710) has a wide tunable wavelength range from 1480 nm to 1640 nm. As illustrated in Fig. 1, the input light ($\sim$ 1550 nm) is partially reflected and forms a well-defined FPI. In the sensor structure, the attached gold film has a nanometer-scale thickness of about 130 nm, which contributes to a large ultrasonic-induced deformation and thus a high ultrasonic sensitivity. Thus, when an acoustic pressure is applied to the FPI, its light behavior is modulated by deforming the ultra-thin gold film. When the driving voltage of the function generator reaches its maximum value of 400 V, the sensor still works well and no film damage occurs in the long-run. In this sense, our work can suit the topic content of nanophotonics, which is the study of the behavior of light on a nanometer scale, and of the interaction of nanometer-scale objects with light.[38–41]

The gold film-based fiber-optic FPI was first reported for SPM imaging in our previous work.[22] Afterwards, we proposed the approach to acoustic focusing to improve its ultrasonic sensitivity in a separate report,[18] in which a plano-concave acoustic focusing lens was located behind the gold film and effectively focused UWs onto it. This improved approach showed an increased ultrasonic sensitivity with an SNR of 64.24 dB. Currently, just by adding a short section of MMF into the FP cavity as a beam collimator, the fringe visibility of the interference spectrum is enhanced with a larger spectral slope, leading to highly sensitive spectral sideband filtering and thus an increased ultrasonic sensitivity with an SNR of 63.8 dB. Although the two approaches have comparable response sensitivities, the one using beam collimation benefits the sensor with easier fabrication and a more compact size, which has no influence on the sensor dimension. However, an additional plastic ferrule was needed to fix the acoustic focus lens in Ref. [18], both of which enlarged the sensor size and reduced the spatial resolution. Recently, another similar diaphragm-based FPI using beam collimation was reported for SPM imaging.[42] Although the acoustic performance was improved, the ultrasonic sensitivity was not high enough and the whole ultrasonic imaging process needed to be implemented in water due to the large acoustic attenuation loss in air. According to Eq. (6), the ultra-thin gold film with a thickness of 130 nm contributes to a higher wavelength-referenced acoustic pressure sensitivity than that with the 30-μm-thick diaphragm used in Ref. [42] . Therefore, despite that the approach to improving the spectral fringe visibility is similar, our sensor has a significantly higher ultrasonic sensitivity and enables the detection of weak UWs in air, which largely simplifies the SPM imaging system.

Furthermore, the SNR of the proposed FPI is much larger than that of our other approaches (27.96 dB for a fiber Bragg grating FP probe,[43] 45.2 dB for a 353ND diaphragm-based FPI,[27] 24.08 dB for a micro-bubble FPI,[44] and 34.8 dB for a Michelson interferometer fixed in a titled tube[12]). The results clearly reveal that the proposed FPI has a considerable response to ultrasonic fields.

Eventually, the structural interfaces of two SPMs are imaged clearly in air by reconstructing the time-of-flight difference of the reflected UWs. The high-precision imaging of SPMs is mainly determined by several factors in the experi-

ments. The key factor is the MMF, as a beam collimator to improve the spectral fringe visibility, which ensures that the sensor has a high ultrasonic sensitivity. Second, the compact size and detection aperture of the sensor provide a fine spatial resolution, particularly for the detection of small defects in SPMs. The final factor is the noise removal. A bandpass filter ranging from 100 kHz to 1 MHz is used to shield noise from the surrounding electromagnetic interference and the PZT resonance harmonics. Besides, the digital filtering is employed for denoising, including extra noise from the mode conversion in SPMs (such as the nonuniformity induced refraction and acoustic velocity change) and additional surface reflections of the surrounding objects (such as the tank walls). Finally, based on the imaging results of two SPMs, the sensor provides a fine spatial resolution of about 1.53 mm. The structural interfaces and small defects in SPMs can be distinguished clearly. Thus, the proposed sensor can be a good candidate to replace PZTs and previous fiber-optic sensors for high-sensitivity and high-precision SPM imaging with easy fabrication and compact size.

5. Conclusion and perspectives

In this paper, a sensitivity-improved fiber-optic FPI is proposed and used for ultrasonic imaging of SPMs in air. By adding a graded-index MMF into the FP cavity for beam collimation, the fringe visibility of the interference spectrum is significantly improved, leading to an increased spectral slope for highly sensitive sideband filtering interrogation. The acoustic performances of the collimated FPI to 300 kHz UWs are experimentally demonstrated and 2D images of two SPMs are reconstructed with a spatial resolution of 1.53 mm. Compared with previous similar approaches, the proposed sensor responds sensitively to UWs and enables high-precision SPM imaging with easy fabrication and compact size.

References

[1] Lamont M R E, Okawachi Y and Gaeta A L 2013 *Opt. Lett.* **38** 3478
[2] Bakulin A, Grechka V and Tsvankin I 2000 *Geophysics* **65** 1788
[3] Urosevic M, Bhat G and Grochau M H 2012 *Geophysics* **77** WC123
[4] Jones C H, Reeg H, Zandt G, Gilbert H, Owens T J and Stachnik J 2014 *Geosphere* **10** 505
[5] Dou S, Nakagawa S, Dreger D and Ajo-Franklin J 2016 *Geophysics* **81** WA233
[6] Park S and He S 2012 *Ultrasonics* **52** 880
[7] Yamashita K, Nishiumi T, Arai K, Tanaka H and Noda M 2015 *Procedia Eng.* **120** 1205
[8] Culshaw B, Thursby G, Betz D and Sorazu B 2008 *IEEE Sens. J.* **8** 1360
[9] Shao L, Lau S, Dong X, Zhang A, Chan H L W, Tam H Y and He S 2008 *IEEE Photon. Technol. Lett.* **20** 548
[10] Beard P C, Hurrell A M and Mills T N 2000 *IEEE Trans. Ultrason. Ferroelectr. Freq. Control* **47** 256
[11] Guo J, Xue S, Zhao Q and Yang C 2014 *Opt. Express* **22** 19573
[12] Gang T, Hu M, Qiao X, Li J, Shao Z, Tong R and Rong Q 2017 *Opt. Laser Eng.* **88** 60
[13] Cranch G A, Johnson L, Algren M, Heerschap S, Miller G A, Marunda T S and Holtz R L 2017 *Opt. Express* **25** 19457
[14] Li Y, Wang X and Bao X 2011 *Appl. Opt.* **50** 1873
[15] Chen R, Fernando G F, Butler T and Badcock R A 2004 *Meas. Sci. Technol.* **15** 1490
[16] Wild G and Hinckley S 2008 *IEEE Sens. J.* **8** 1184
[17] Guo F, Fink T, Han M, Koester L, Turner J and Huang J 2012 *Opt. Lett.* **37** 1505
[18] Rong Q, Zhou R, Hao Y, Yin X, Shao Z, Gang T and Qiao X 2017 *IEEE Photon. J.* **9** 6802511
[19] Ma J, Xuan H, Ho H, Jin W, Yang Y and Fan S 2013 *IEEE Photon. Technol. Lett.* **25** 932
[20] Xu J, Wang X, Cooper K L and Wang A 2005 *Opt. Lett.* **30** 3269
[21] Morris P, Hurrell A, Shaw A, Zhang E and Beard P 2009 *J. Acoust. Soc. Am.* **125** 3611
[22] Rong Q, Hao Y, Zhou R, Yin X, Shao Z, Liang L and Qiao X 2017 *Sensors* **17** 397
[23] Xu F, Shi J, Gong K, Li H, Hui R and Yu B 2014 *Opt. Lett.* **39** 2838
[24] Li M, Wang M and Li H 2006 *Opt. Express* **14** 1497
[25] Gong S C and Lee C 2001 *IEEE Sens. J.* **1** 340
[26] Eaton W P and Smith J H 1997 *Smart Mater. Struct.* **6** 530
[27] Zhang W, Wang R, Rong Q, Qiao X, Guo T, Shao Z, Li J and Ma W 2017 *IEEE Photon. J.* **9** 7103208
[28] Li Z, Pei L, Dong B, Ma C and Wang A 2012 *Appl. Opt.* **51** 4709
[29] Zhang E and Beard P 2006 *IEEE Trans. Ultrason. Ferroelectr. Freq. Control* **53** 1330
[30] Wang R, Liu Z and Qiao X 2016 *Sens. Actuators B Chem.* **234** 498
[31] Zhang Y, Li Y, Wei T, Lan X, Huang Y, Chen G and Xiao H 2010 *IEEE Photon. J.* **2** 469
[32] Wang R, Zhang J, Weng Y, Rong Q, Ma Y, Feng Z, Hu M and Qiao X 2013 *IEEE Sens. J.* **13** 1766
[33] Rong Q, Qiao X, Du Y, Feng D, Wang R, Ma Y, Sun H, Hu M and Feng Z 2013 *Appl. Opt.* **52** 1441
[34] Du Y, Qiao X, Rong Q, Yang H, Feng D, Wang R, Hu M and Feng Z 2014 *IEEE Sens. J.* **14** 1069
[35] Xu J, Pickrell G, Wang X, Peng W, Cooper K and Wang A 2005 *IEEE Photon. Technol. Lett.* **17** 870
[36] Beard P C and Mills T N 1996 *Appl. Opt.* **35** 663
[37] Shao Z, Rong Q, Chen F and Qiao X 2018 *Opt. Express* **26** 10820
[38] Zhang Y, Lin B, Tjin S C, Zhang H, Wang G, Shum P and Zhang X 2010 *Opt. Express* **18** 26345
[39] Yang S, Liu Y, Chen W, Jin W, Zhou J, Zhang H and Zakharova G S 2016 *Sens. Actuators B* **226** 478
[40] Wang T, Guo Y, Wan P, Zhang H, Chen X and Sun X 2016 *Small* **12** 3748
[41] Xiang Y, Dai X, Guo J, Zhang H, Wen S and Tang D 2015 *Sci. Rep.* **4** 5483
[42] Zhang W, Chen F, Ma W, Rong Q, Qiao X and Wang R 2018 *Opt. Express* **26** 11025
[43] Rong Q, Shao Z, Yin X, Gang T, Liu F, Sun A and Qiao X 2017 *IEEE J. Sel. Top. Quantum Electron.* **23** 5600506
[44] Gang T, Hu M, Rong Q, Qiao X, Liang L, Liu N, Tong R, Liu X and Bian C 2016 *Sensors* **16** 2125